

# A minimal electrical model of the human heart

João Olívia, Rui Dilão

University of Lisbon, Instituto Superior Técnico, Dep. Physics  
Av. Rovisco Pais, 1049-001 Lisbon, Portugal

March 26, 2025

## Abstract

We develop a minimal whole-heart model that describes cardiac electrical conduction and simulate a basic three-lead electrocardiogram (ECG). We compare our 3-lead ECG model with clinical data from a database of Norwegian athletes. The results demonstrate a strong correlation with the ECGs recorded for these athletes. We simulate various pathologies of the heart's electrical conduction system, including ventricular tachycardia, atrioventricular nodal reentrant tachycardia, accessory pathways, and ischemia-related arrhythmias, demonstrating that the 3-lead ECGs align with the clinical data. This minimal model serves as a computationally efficient digital twin of the heart.

**Keywords:** Whole-heart model, Whole-heart digital twin, ECG simulations, arrhythmias, tachycardias, accessory pathways.

## 1 Introduction

Whole-heart modelling has developed significantly in recent years [Bueno-Orovio *et al.*, 2008]. Efforts in action potential modelling, combined with advances in optical imaging, have enabled researchers to explore the creation of in silico versions of human hearts, including those of specific patients, utilising them as predictive and diagnostic tools. Initially, in silico heart models may not aim to replicate a specific heart but rather to construct a generic one, thereby reducing the need for animal experimentation [Trayanova, 2011]. Conversely, precision medicine—where therapies are custom-designed for each patient—relies heavily on the ability to develop digital twins, rendering the data from a specific patient critically important. By integrating the wealth of information obtained from various examinations, such as echocardiography, magnetic resonance imaging, ECG, genetic testing, and blood pressure measurements, alongside knowledge of physics and physiology, it becomes possible to create computationally robust models that can replace traditional empirical diagnostic tools [Gillette *et al.*, 2022]. These models offer quantitative insights into the underlying causes of specific symptoms. Numerous research groups have initiated and are currently pursuing such projects. For instance, the work carried out in the Trayanova lab utilises imaging tools to create a digital twin, which is subsequently employed to predict the optimal ablation sites for patients affected by Arrhythmogenic Right Ventricular Cardiomyopathy [Niederer *et al.*, 2022]. The research conducted by Viola and colleagues highlights the computational power required for these approaches by utilising the processing capabilities of GPUs in the development of digital twins [Viola *et al.*, 2023]. A review by [Thangaraj *et al.*, 2023] outlines the significant potential of digital twin development, along with the challenges associated with its implementation in clinical environments.

Several models have been developed to describe the propagation of action potential signals along cardiac tis-

sues. The first model was introduced in 1962 by Denis Noble as a modified version of the Hodgkin-Huxley neuronal model [Noble, 1962]. Additional models depicting action potentials in various heart cells have been published for both human and animal hearts [Irisawa & Noma, 1982, Courtemanche *et al.*, 1998]. Over the years, more detailed models have emerged, the vast majority of which are available at the CellML model repository (<https://www.cellml.org>). These models are typically categorised into three generations, each with increasing complexity. The first-generation models, exemplified by the Beeler-Reuter model, include a limited number of ion channels such as  $\text{Na}^+$ ,  $\text{K}^+$ , and  $\text{Ca}^{2+}$  and consist of fewer than 10 differential equations [Beeler & Reuter, 1977]. The inclusion of  $\text{Ca}^{2+}$  was a crucial milestone, as this ion is primarily responsible for the electromechanical coupling essential to the heart's function. The second-generation models increase the number of ion channels from 10 to 20 and the differential equations from 20 to 40. The third-generation models currently under development are significantly more complex, taking into account specific biological processes and dynamics. Although the trend has been towards increasingly complex models, [Quarteroni *et al.*, 2022, Fedele *et al.*, 2023], simplified variants still yield significant results, such as the ventricular action potential developed by [Bueno-Orovio *et al.*, 2008].

In this paper, we develop a minimal whole-heart model, where the basic anatomy of the heart is described with minimal details to ensure computational efficiency. In section 2, we model the four heart cavities as four two-dimensional square domains with appropriate boundary conditions. Each square domain contains a lattice of points representing heart cells (myocytes). Each cell communicates with its neighbouring cells. Anatomical structures such as valves and nodal points are included to facilitate the analysis of connectivity and electrical conduction through the heart. In section 3, we introduce a simplified two-dimensional Hodgkin-Huxley model that characterises

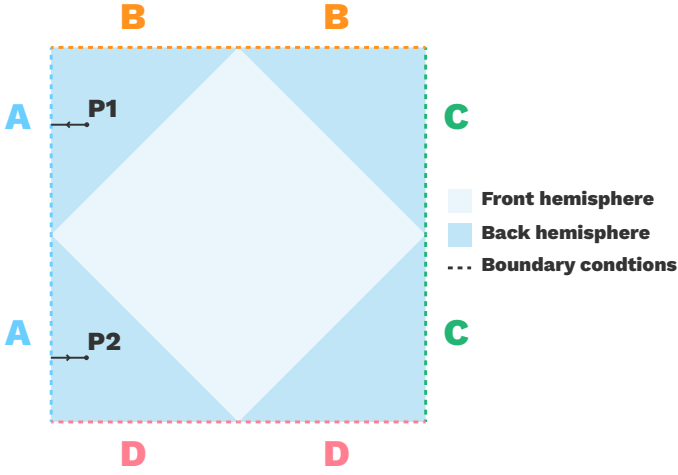


Figure 1: 2D a map (chart) of a spherical surface is utilised to simulate the heart cavities. The sides displaying the same letter are cell-identified. The front and back hemispheres of the spherical surface are distinguished by lighter and darker shades of blue, respectively.

the electrical states of the human heart, which propagate through the cell lattices. In section 4, we simulate the complete cycle of a healthy heart, demonstrating that the fundamental electrophysiological properties are present in the model. In section 5, we reconstruct the first three leads of an ECG, comparing it with clinical data. In section 6, we simulate several heart pathologies, including ventricular tachycardia, atrioventricular nodal reentrant tachycardia, accessory pathways, and ischemia-related arrhythmias. Finally, in section 7, we summarise the main results of the paper.

## 2 The anatomical geometry of the human heart

One of the most important concepts underlying this work is how we will spatially model the heart. For each approximately spherical heart cavity, a two-dimensional squared domain with the appropriate boundary conditions will be employed, representing the surface of a sphere. Each surface will depict the muscular tissue with cells arranged in a squared lattice. Each point of the square lattice represents a cell characterised by different parameter values and electrical states.

In figure 1, the projection of the spherical surface is shown. Each side of the square is labelled with a letter from A to D and is divided into two halves. The lattice points in the halves sharing the same letter are identified. This leads to a two-dimensional surface that is homeomorphic to a two-dimensional sphere. In mathematical terms, this construction represents a chart of the 2-sphere [Dilão, 2023, Appendix A.1.2].

The four heart cavities will be represented by four similar squares discretised into  $76 \times 76$  squared lattices. With this geometry serving as the fundamental component of our heart model, we now outline each of the heart's cavities along with their respective anatomical structures and connections.

The coordinate system used to locate each heart cell

or myocyte is  $P_{\text{Structure}} = (x, y)_{\text{Cavity}}$ , where  $(x, y)$  denotes the two-dimensional integer coordinates of the lattice points in the heart cavities: Right Atrium (RA), Left Atrium (LA), Right Ventricle (RV), and Left Ventricle (LV). The origins of the coordinates are at the top-left vertices of each square lattice. Heart cavities are connected by linear chains or bundles of cells and are referenced as  $P_{\text{bundle}} = (x)_{\text{bundle}}$ , where  $x$  is the number of cells in the chain.

In figure 2, the final geometry of the whole heart is displayed. The diamond-shaped lines act as references for the front and back hemispheres, similar to what was presented in figure 1.

The Right Atrium is characterised by the presence of three zero-flux anatomical structures. These structures comprise the Superior and Inferior Vena Cavas (SVC and IVC), represented by squares with a side length of  $a = 8$ . Their fixed central positions are  $P_{\text{SVC}} = (25, 8)_{\text{RA}}$  and  $P_{\text{IVC}} = (15, 60)_{\text{RA}}$ , along with the Tricuspid Valve (TV), modelled as a rectangle with dimensions  $13 \times 26$ , situated at the bottom centre of the square. The boundaries of these three anatomical structures are characterised by zero-flux boundary conditions. The Sinoatrial Node (SAN) is placed at  $P_{\text{SAN}} = (19, 19)_{\text{RA}}$ . The BACH1 and BACH2 points connects the right to the left atria, simulating the Bachmann's Bundle,  $P_{\text{BACH1}} = (30, 25)_{\text{RA}}$  and  $P_{\text{BACH2}} = (19, 19)_{\text{LA}}$ . The electrical states of BACH1 and BACH2 are the same. The Atrioventricular Node (AVN) with coordinates  $P_{\text{AVN}} = (57, 57)_{\text{RA}}$  connects to the first point of the BUNDLE1, responsible for the linear connection between atria and ventricles, simulating the His and bundle.

Within the Left Atrium, the Pulmonary Veins (PV) are represented as zero-flux squares with a side length of  $a = 8$ , situated at  $P_{\text{PV1}} = (13, 13)_{\text{LA}}$ ,  $P_{\text{PV2}} = (63, 13)_{\text{LA}}$ ,  $P_{\text{PV3}} = (13, 63)_{\text{LA}}$ , and  $P_{\text{PV4}} = (63, 63)_{\text{LA}}$ . The Mitral Valve (MV) is placed at the bottom centre of the LA.

The connection between the atria and ventricles in the human heart occurs through three primary structures: the His bundle, the bundle branches, and the Purkinje fibres. For the sake of simplicity, we have described these structures using a single channel, referring to it as *bundle*. This structure varies in length depending on the heart rate.

Within the bundle,  $P_{\text{BUNDLE1}} = (1)_{\text{bundle}}$  connects directly to the AVN, while  $P_{\text{BUNDLE2}} = (60)_{\text{bundle}}$ ,  $P_{\text{BUNDLE3}} = (80)_{\text{bundle}}$ , and  $P_{\text{BUNDLE4}} = (90)_{\text{bundle}}$  are connected to the ventricles RV1/LV1, RV2/LV2, and RV3/LV3, respectively. These points were specifically chosen to model the path taken by the Purkinje fibres across the ventricular tissue. The points  $P_{\text{RV1}} = (57, 19)_{\text{RV}}$  and  $P_{\text{LV1}} = (19, 19)_{\text{LV}}$  are located at the interventricular septum, which is the first region excited by the Purkinje fibres. The points  $P_{\text{RV2}} = (38, 76)_{\text{RV}}$  and  $P_{\text{LV2}} = (38, 76)_{\text{LV}}$  represent the apex of the ventricles, while  $P_{\text{RV3}} = (19, 19)_{\text{RV}}$  and  $P_{\text{LV3}} = (57, 19)_{\text{LV}}$  signify the base of the ventricles.

Similar to the atria, the ventricles possess non-conducting regions that represent the valves; however, in this instance, they also signify the obstruction caused by the Pulmonary Artery (PA) and the Aorta (AO) for the right and left ventricles, respectively.

Alongside the basic structure of the heart previously described, a ventricular epicardial layer was incorporated

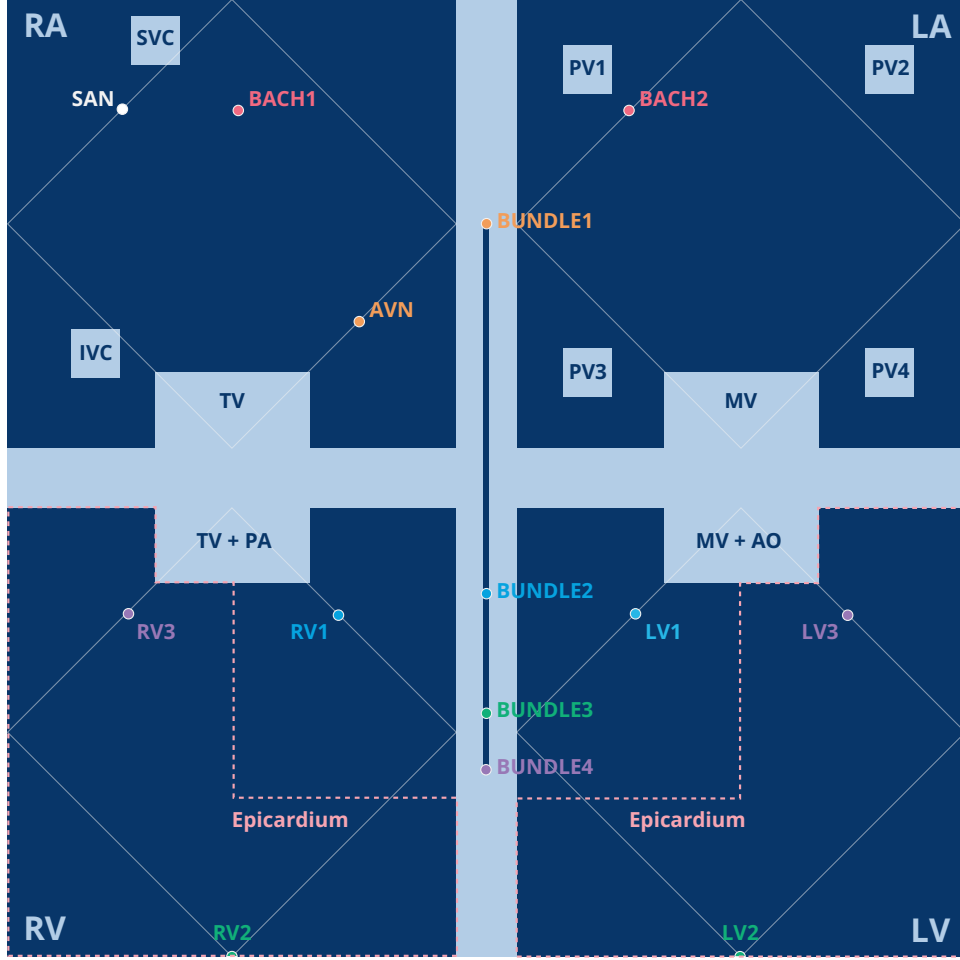


Figure 2: Spherical surface (chart) of the whole heart with its four cavities: right and left atria and ventricles. BACH1 and BACH2 are the connection points for the two atria, simulating Bachmann’s bundle, which in this model is reduced to a point. The bundle line connects the atria to the ventricles. The Atrioventricular Node (AVN) connects to the bundle points BUNDLE1. The bundle points BUNDLE2, BUNDLE3, and BUNDLE4 connect to RV1/LV1, RV2/LV2, and RV3/LV3, respectively, simulating the His and Purkinje fibres. The dashed lines indicate the boundaries of the ventricular epicardial layers, added to account for the thickness of the ventricular walls.

into the aforementioned ventricular layers to ensure the correct direction of ventricular repolarisation, which will be analysed in the next section. In human ventricles, the outer layer of the muscular walls, the epicardium, exhibits shorter action potentials compared to the myocardium and the endocardium. Consequently, the last cells to depolarise are the first to repolarise, resulting in the repolarisation wavefront being opposite to the depolarisation wavefront. The boundaries of these epicardial layers are delineated across the ventricles with orange dashed lines. They do not form complete spheres as they do not encircle the ventricles in the interventricular septum region. Each ventricular layer is vertically connected to its corresponding epicardial layer; that is, each cell on one layer is linked to the cell with the same coordinates on the other layer.

### 3 Propagation of the electrophysiological stimulus

The model equations that describe how the electric stimulus propagates through the cardiac cells are an adapted Hodgkin-Huxley (HH) reaction-diffusion model in two spatial dimensions, controlled exclusively by a potassium-sodium gating variable ([Branco & Dilão, 2024]). The choice of this adapted version of the model over the original four-dimensional HH model relates to the overall intention of simplicity. The model’s reaction-diffusion partial differential equations are

$$\begin{cases} C_m \frac{dV}{dt} &= I + D \left( \frac{\partial^2 V}{\partial x^2} + \frac{\partial^2 V}{\partial y^2} \right) - g_K n^4 (V - V_K) \\ &\quad - g_{Na} m_\infty^3 (c(I) - n) (V - V_{Na}) \\ \frac{dn}{dt} &= \alpha_n(V)(1 - n) - \beta_n(V), \end{cases} \quad (1)$$

where

$$\begin{aligned}
m_\infty &= \frac{\alpha_m(V)}{\alpha_m(V) + \beta_m(V)} \\
\alpha_m(V) &= 0.1\phi \frac{V + 25}{e^{(V+25)/10} - 1} \\
\beta_m(V) &= 4\phi e^{V/18} \\
\alpha_n(V) &= 0.01\phi \frac{V + 10}{e^{(V+10)/10} - 1} \\
\beta_n(V) &= 0.125\phi e^{V/80} \\
c &= \begin{cases} 1.0 & \text{for } I \in [0, 2) \\ 1.046I^{-0.077} & \text{for } I \in [2, 160], \end{cases}
\end{aligned}$$

and  $n$  represents the potassium-sodium gating variable. We selected  $C_m = 50 \mu\text{F}/\text{cm}^2$  for the transmembrane capacitance. The Nernst potentials for both sodium and potassium channels are  $V_{Na} = -115 \text{ mV}$  and  $V_K = -12 \text{ mV}$ . The conductances for sodium and potassium channels are  $g_{Na} = -120 \text{ mS}/\text{cm}^2$  and  $g_K = 36 \text{ mS}/\text{cm}^2$ , respectively, and  $\phi = 1$ . For a model with more gating variables, see [Alonso *et al.*, 2016].

For myocytes, the current in equation (1) is set to  $I = 0 \mu\text{A}/\text{cm}^2$ . The oscillation period of the SAN relates to the input current  $I$  through the expression  $T(I_{SAN}) = 1.7I_{SAN}^{-0.45}$  s, such that the standard heartbeat of 60 bpm ( $T = 1 \text{ s}$ ) is achieved by setting  $I_{SAN} = 2.95 \mu \text{ A}/\text{cm}^2$  ([Branco & Dilão, 2024]).

The equations (1) were discretised and numerically solved using a forward-Euler method. The diffusion coefficients, which describe the propagation along the myocytes, were calibrated according to the relation  $D\Delta t/\Delta x^2 = 1/6$ , where  $\Delta t$  is the integration time step and  $\Delta x$  is the spatial scale of the cavity point lattices. Additionally,  $D = \Delta x^2/R$ , where  $R$  is the resistivity parameter characterising the heart tissue ([Dilão & Sainhas, 1998] and [Branco & Dilão, 2024]).

To ensure that the ventricular AP is longer than the epicardial AP, the potassium channel conductance  $g_K$  in the ventricular layer cells is reduced to create an extended plateau phase. This duration is influenced by heart rate; the faster the oscillation frequency of the sinoatrial node (SAN), the smaller the difference between the AP durations of both layers. The variation in the interval between depolarisation and repolarisation of the ventricles as a function of heart rate has been well studied. Numerous expressions have been proposed over the years to adjust the QT ECG interval for various heart rates, a concept known as the QTc (corrected QT interval). Here, we have employed the expression

$$g_{Kcorr} = \frac{1}{-0.018} \left( 0.42 \left( \sqrt[3]{1.7I_{SAN}^{-0.45}} \right) - 0.724 \right)$$

adapted from [Fridericia, 1920] and [Branco & Dilão, 2024]. For a heart rate of 60 bpm, the potassium channel conductances in the ventricular layer cells are set at  $g_{Kcorr} = 16.54 \text{ mS}/\text{cm}^2$ , whereas all other cells, including those in the epicardial layer, maintain the standard value of  $g_K = 36 \text{ mS}/\text{cm}^2$ .

With regard to the propagation of the AP along the bundle, we have assumed that the length of the bundle is

$$l_{bundle} = 0.7 \left( -0.69 \left( \frac{60}{1.7I_{SAN}^{-0.45}} - 60 \right) + 85.7 \right) + 30$$

rounded to the nearest integer. This is based on the observation that, in a control group, an increase of 6.9 ms was observed in the interval between atrial and ventricular depolarisation for every 10-beat increase in heart rate, thereby indicating a linear relationship between the two [Atterhög & Loogna, 1977].

## 4 Dynamics of the whole heart

Having established the geometry of all the heart cavities and their interconnections, we now simulate the temporal evolution of the AP in a healthy whole heart. The temporal evolution of the whole heart's electrophysiological state has been simulated in Python and is available on GitHub ([Olívia & Dilão, 2025]). In all the simulations presented in this paper, we have chosen  $\Delta t = 0.375 \text{ ms}$  for the numerical integration of equations (1). The spatial scale is  $\Delta x = 0.93 \text{ mm}$  to accommodate for heart dimensions. Other parameters for a healthy heart with a heart rate of 60 bpm are shown in Table 1.

In figure 3, we present 15 frames from a complete heart-beat, carefully selected to illustrate the critical stages of each cycle. This heartbeat begins at  $t = 253 \text{ ms}$ , when the stimulus from the SAN propagates to the adjacent cells. At  $t = 273 \text{ ms}$ , the signal reaches the left atrium through the connection from the BACH1 to the BACH2 point. The signal then arrives at the AVN and spreads to the BUNDLE1 point at  $t = 330 \text{ ms}$ . As the excitation continues to advance through the bundle, the atria begin to repolarise, depicted by the progression of the blue wavefront from  $t = 422 \text{ ms}$  to  $t = 465 \text{ ms}$ . At  $t = 454 \text{ ms}$ , the signal reaches the first contact points with the ventricles, the RV1 and LV1 points, initiating the ventricles' depolarisation. As the signal reaches the tenth to last cell of the bundle, at  $t = 454 \text{ ms}$ , the RV2 and LV2 points depolarise, propagating the signal from the apex of the ventricles. At  $t = 465 \text{ ms}$ , the signal arrives at the final contact point between the bundle and the ventricles, and the excitation emanates through the RV3/LV3 points. From just after  $t = 525 \text{ ms}$  to just before  $t = 645 \text{ ms}$ , the ventricular myocytes are in the extended plateau phase made possible by the differing potassium conductance of  $g_K = 16.5 \text{ mS}/\text{cm}^2$ . At  $t = 645 \text{ ms}$ , the epicardium, which is not displayed but is understood to be atop the ventricular layers, commences repolarisation at the apex and then at the base, propagating this depolarisation to the RV2/LV2 and RV3/LV3 points. This repolarisation then continues in opposition to the primary depolarisation wave that originated at  $t = 454 \text{ ms}$  until the end of the cycle at  $t = 822 \text{ ms}$ .

A plot of the action potentials of selected cells is presented in Figure 4. Each line represents the action potential of a point of interest during each heartbeat. The signal originates at the SAN travels through the BACH1–BACH2 point to the LA. Subsequently, it arrives at the atrioventricular node (AVN), which propagates the signal to the bundle. After passing through the bundle, the signal is dispersed throughout the ventricles. The first red line indicates the cell  $(19, 19)_{LV}$  (the top leftmost point of the left ventricle), which is the first to excite. The cell at the centre of the frontal hemisphere,  $(38, 38)_{LV}$ , experiences depolarisation, followed by the bottom leftmost cell

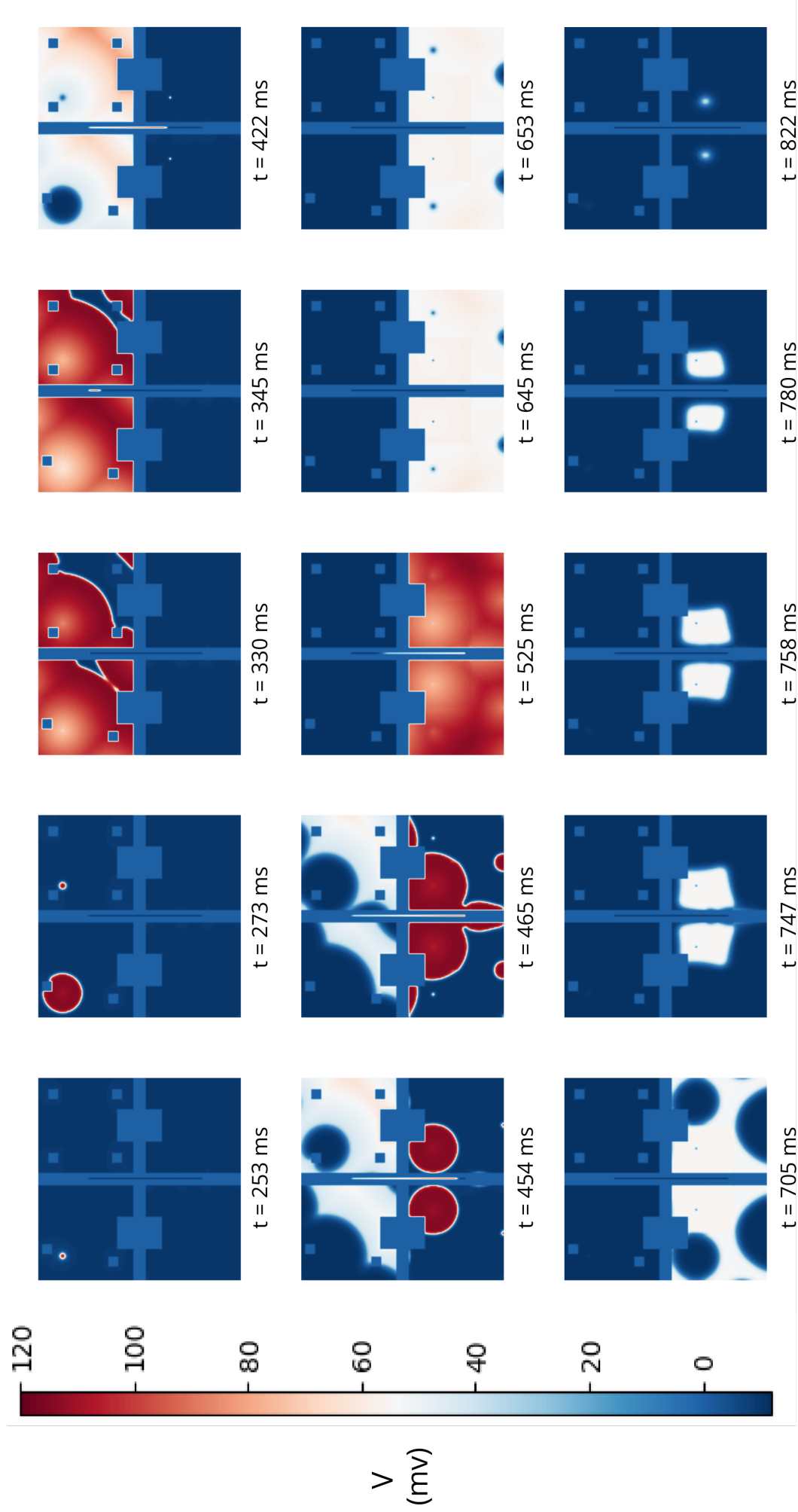


Figure 3: Propagation of the membrane potential across the four heart chambers, calculated using the model equations (1), during a single heartbeat at a heart rate of 60 bpm. The AP signal originates at the SAN at time  $t = 253$  ms. Each frame provides a complete view of the heart.

Table 1: Initial conditions and parameters used in the simulation of the heartbeat of a healthy heart with a frequency of 60 bpm.

cells	$V(t=0)$ (mV)	$n(t=0)$	$I$ ( $\mu\text{A}/\text{cm}^2$ )	$g_K$ (mS/cm <sup>2</sup> )	$R$ (k $\Omega\text{cm}^2$ )
$P_{\text{SAN}} = (19, 19)_{\text{RA}}$	-10.95	0.17	2.95	36	0.00675
Ventricle cells	-10.95	0.17	0	16.54	0.00675
All other cells	-10.95	0.17	0	36	0.00675

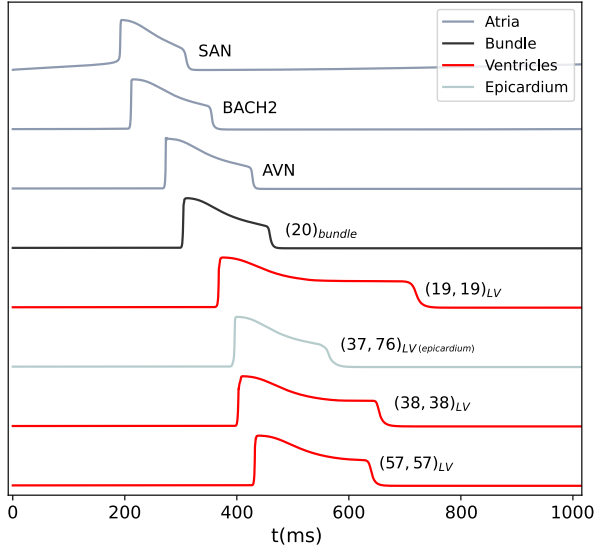


Figure 4: Action potential time profiles at selected heart cells. The darker grey corresponds to atrial cells, the black corresponds to a bundle cell, the red corresponds to ventricle cells, and the light grey corresponds to an epicardial cell.

at  $(57, 57)_{\text{LV}}$ . A key characteristic of these three APs of the left ventricle (LV) cells is their repolarisation. The later a cell is excited, the earlier it begins to repolarise, as demonstrated by the differences among these three APs. These dynamics explain why the T-wave is an upright deflection in leads I and II, a phenomenon made possible by the presence of the epicardial layers. The light blue line, representing an epicardial cell, illustrates that the AP duration in epicardial cells is similar to that of atrial myocytes, while the longest AP in the ventricles is approximately twice as long. The complete dynamics of the epicardial layer will be discussed in the following section.

## 5 The Electrocardiogram

The electrocardiogram serves as the benchmark by which we assess the clinical validity of our model. Electrodes placed on a patient's skin measure the local flow of ions resulting from the electrical field generated in the heart [Enderle & Bronzino, 2012]. The electrical impulse travels through the extra myocardial region, which consists of resistive tissue and fluid surrounding the heart within the human body, while the potential difference captured by the electrodes is reflected in an ECG.

We measure the differences in membrane potential  $V$  between pairs of neighbouring cells based on the ECG lead position. This method accounts for the average electrical field generated in the heart in each spatial direction. The

expressions for the first three leads of the ECG are

$$\langle \Delta V_{\text{ECG}}^I(t) \rangle = -\frac{1}{N_{\text{total}}} \sum_{i=1}^4 \alpha_i \sum_{(x,y) \in \Omega_f} z_{(x,y)} \cdot (V_{(x+1,y+1)}^t - V_{(x,y)}^t) \quad (2)$$

$$\langle \Delta V_{\text{ECG}}^{II}(t) \rangle = -\frac{1}{N_{\text{total}}} \sum_{i=1}^4 \alpha_i \sum_{(x,y) \in \Omega_f} z_{(x,y)} \cdot (V_{(x,y+1)}^t - V_{(x,y)}^t) \quad (3)$$

$$\langle \Delta V_{\text{ECG}}^{III}(t) \rangle = \frac{1}{N_{\text{total}}} \sum_{i=1}^4 \alpha_i \sum_{(x,y) \in \Omega_f} z_{(x,y)} \cdot (V_{(x+1,y)}^t - V_{(x,y)}^t), \quad (4)$$

where

$$z_{(x,y)} = \sqrt{\left(\frac{l}{2}\right)^2 - \left(x - \frac{l}{2}\right)^2 - \left(y - \frac{l}{2}\right)^2}$$

and the subscripts in the membrane potential  $V(t)$  indicate the cell coordinates  $(x, y)$ .  $\Omega_f$  denotes the set of all cells in the front hemisphere of each heart cavity, comprising  $N_{\text{total}}$  cells, and  $\alpha_i$  is a scaling coefficient unique to each heart cavity. The atria and ventricles possess different muscle masses, thus demonstrating distinct contributions to the heart's electrical signature. In this context, a simple coefficient is employed to differentiate the contributions of each cavity. The index  $i$  designates each cavity, with  $i = 1, 2, 3, 4$  corresponding to the RA, LA, RV, and LV, respectively. Anatomical data informed the values assigned to these coefficients, considering wall thickness and surface area. The selected values are  $\alpha_1 = \alpha_2 = 1$ ,  $\alpha_3 = 5$ , and  $\alpha_4 = 15$ , ensuring both atria contribute similarly while the ventricles possess ten times the muscle mass of the atria. The weight parameter  $z_{(x,y)}$  is a correction due to the curvature of the heart. The constant  $l$  is defined as the side length of each cavity,  $l = 76$  cells. As the cardiac muscle is disposed of in an approximately spherical shape around the cavities, muscle walls' surfaces will contribute differently to the potential difference measured in each ECG electrode. The weight parameter  $z_{(x,y)}$  ensures that each cell's contributions to the ECG signal reflect this geometry.

There is symmetry between the front and back hemispheres, aside from the arteries and veins, which do not interfere with the propagation direction of the AP signal. Therefore, computing the ECG on both sides of the cavities would be redundant.

Figure 5 illustrates the simulation results of an ECG obtained using equations (2)-(4), compared with the ECG of athlete number 5 from the Norwegian Endurance Athlete ECG database [Singstad, 2022]. A heart rate of 50 bpm was chosen for the simulated heart to align with that of the athlete.

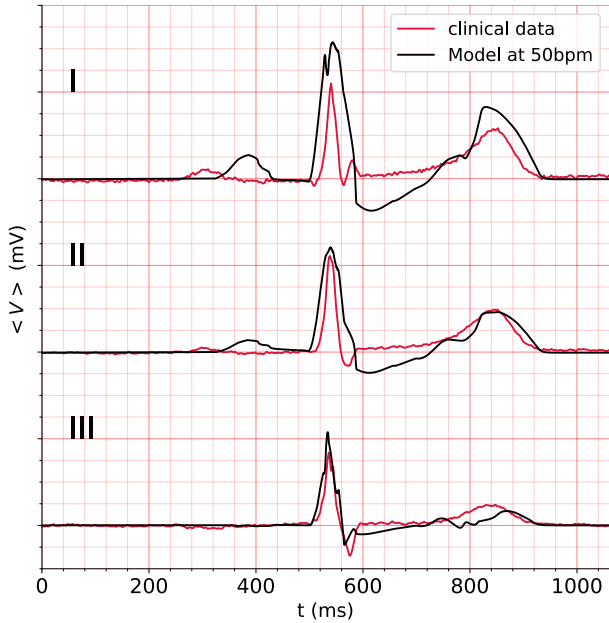


Figure 5: In red, we present the 3-lead ECG of an athlete with a heart rate of 50 bpm. In black, we depict the model simulation obtained with  $I_{SAN} = 2.2 \mu\text{A}/\text{cm}^2$ . Each small square measures 0.2 mV along the vertical direction and 40 ms in the horizontal direction.

According to the database, this athlete presents with sinus bradycardia, sinus arrhythmia, and first-degree AV block, but he has an otherwise normal ECG. We observe considerable agreement when comparing the three leads between the results of our model and the clinical data. Both ECGs were aligned to the peaks of the QRS complex, and we particularly note a deviation in the P waves. This deviation can be attributed to the first-degree AV block from which the patient suffers, characterised by PR intervals exceeding 0.2 seconds. In this case, the athlete has a PR interval of 0.26 seconds, while our model indicates a PR interval of 0.18 seconds. Furthermore, finer differences are especially noticeable for leads I and II, not only in the overall shape of the QRS complex but also in the form of the wave marking the QT interval. The absence of a flatter section separating the QRS and the T-wave on our model's ECG can be explained by the shape of the action potential generated by the model equations (1). While the action potential of ventricular myocytes features a flatter plateau phase, characterised by the influx of calcium ions, our model exhibits a much steeper post-depolarisation curve, contributing to changes in potential differences across the ventricles through their action potentials.

## 6 Arrhythmias, accessory pathways and tissue death

### 6.1 Ventricular tachycardia

Ventricular tachycardia is a condition characterised by an increased heart rate, where the signal originates from the ventricle instead of the SAN, often due to spiral waves.

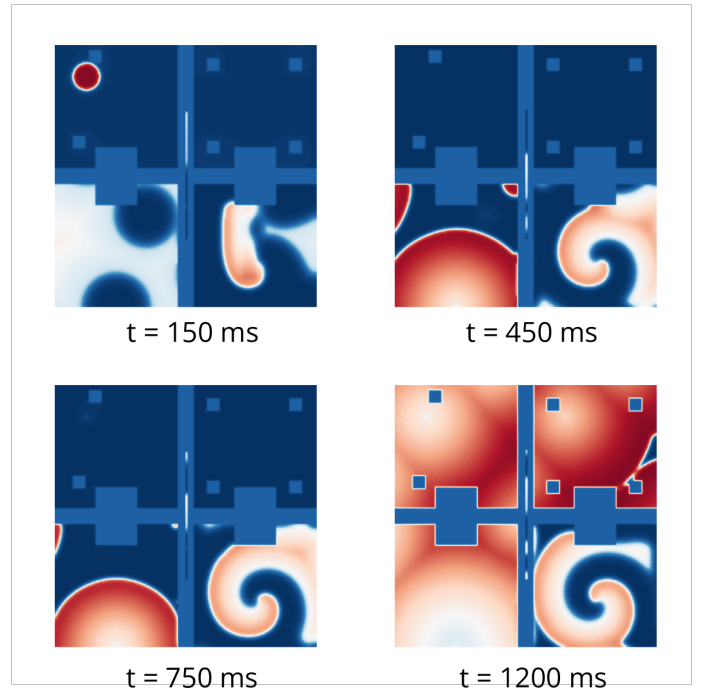


Figure 6: Propagation of the membrane potential where a perturbation in a rectangular region of size  $14 \times 50$  was introduced in the left ventricle, with the initial conditions in Table 2. A permanent spiral develops with a rotating arm.

One possible origin of spiral waves is the appearance of an excited region in the ventricular tissue [Beaumont *et al.*, 1998]. Such dynamics were modelled in our digital organ by setting specific initial conditions to generate a spiral wave in the left ventricle, as shown in Table 2.

Figure 6 shows the evolution of the modelled heart with initial conditions shown in Table 2. A single spiral arm forms in the Left Ventricle due to the initial conditions. The spiral never ends, and reentry keeps occurring.

Displayed in figure 7 is the modelled ECG of the heart shown in figure 6. The shape of the healthy ECG from figure 5 has been supplanted by a roughly homogeneous oscillation. The period of oscillation is now approximately  $T_{vtachy} = 145$  ms, which corresponds to a heart rate of 413 bpm. This is extremely elevated, even for ventricular tachycardias. The wave is not entirely homogeneous; a period-3 pattern is evident from leads II and III, which indicates the activation of the right ventricle. Such activation is not feasible for every spiral rotation due to the refractory period of the connecting cells; the right ventricle activates only after every third rotation of the spiral arm.

This highlights a limitation of our model: the connection between the ventricles. In this work, the connection is established at only three points rather than being continuous. In reality, the ventricles are not electrically isolated from one another; they share the interventricular septum, meaning they are not two separate surfaces like the atria, which connect solely via Bachmann's bundle. Rectifying the connections between the ventricles will remain a task for future work. Were it not for this imprecision, we would expect the ECG to exhibit a monomorphic tachycardia, where each oscillation demonstrates very similar dynamics. Nevertheless, under these conditions, the three leads

Table 2: Initial conditions and parameters for the model of the heart leading to left ventricular tachycardia.

cells	$V(t=0)$ (mV)	$n(t=0)$	$I$ ( $\mu\text{A}/\text{cm}^2$ )	$g_K$ ( $\text{mS}/\text{cm}^2$ )	$R$ ( $\text{k}\Omega\text{cm}^2$ )
$(27 \leq x \leq 28, 16 \leq y \leq 65)_{LV}$	120	0.17	0	36	0.00675
$(29 \leq x \leq 40, 16 \leq y \leq 65)_{LV}$	-10.95	0.99	0	36	0.00675
All other cells	-10.95	0.17	0	36	0.00675

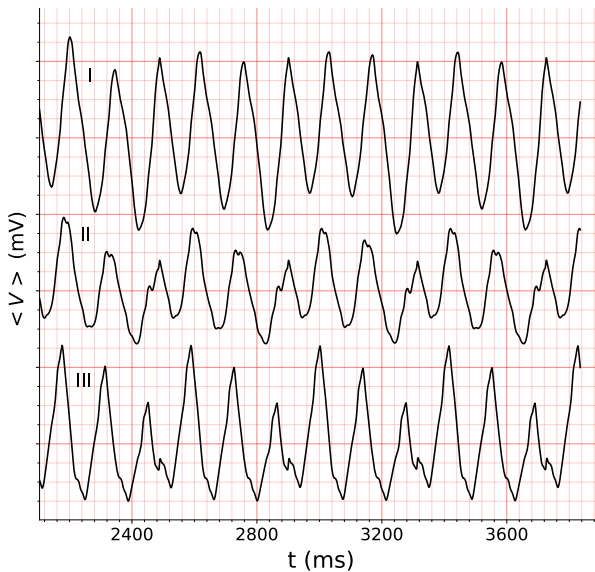


Figure 7: Simulated 3-lead ECG of the heart suffering from ventricular tachycardia shown in figure 6. A non-monomorphic wave is visible due to problems with the connection between ventricles. The period of oscillation of the ECG is approximately  $T_{vtachy} = 145$  ms, contrasting with the period  $T \approx 1000$  ms of our reference healthy heart (60 bpm).

are particularly alike. Due to the rotational nature of the spiral wave, there is no preferred direction in which the signal travels in the left ventricle, which contributes the most to the ECG signature given its size. The amplitude of the waves is also diminished, indicating that not only is the ventricle continuously contracting but that its contractions are also weaker, resulting in ineffective pumping under such circumstances.

## 6.2 Atrioventricular nodal reentry tachycardia

The AVN is not merely a passage between the right atrium and the bundle of His, as modelled for a healthy heart. Rather, as its name suggests, this node is a cluster of cells with specific dynamics. In certain individuals, the AVN possesses two pathways through which the signal can travel: a slower one and a faster one [George *et al.*, 2017]. The cells in the fast pathway have longer refractory periods than those in the slow branch. This, combined with premature excitation in the right atrium, disrupts the symmetry between the two pathways, provided that the premature excitation occurs early enough for the signal to reach the fast pathway while its cells are still recovering from the previous excitation. Consequently, under such conditions, the signal will only travel through the slow path, while no signal will pass through the faster one,

resulting in re-entry in a roundabout effect. New wavefronts no longer originate at the SAN but at the AVN. The PR interval is significantly shorter, and the T-wave and P-wave become overlaid.

To model this mechanism, the slow pathway is modelled by reducing the diffusion coefficient, which does not contribute to the reduced refractory period. Nonetheless, through a more artificial approach, by creating a unidirectional block on one of the cells within the slow branch, we can mimic this behaviour and induce reentry. In figure 9, we illustrate the AVN structure.

The slow pathway has a gap-junction resistivity 33 times higher, with  $R_{slow} = 0.223 \text{ k}\Omega\text{cm}^2$ . The cell at  $P = (6, 2)_{AVN}$  (top left branch) possesses a unidirectional block, indicating that diffusion is obstructed. The top cell of the AVN connects to  $P = (57, 57)_{RA}$  (the original position of the AVN), and the bottom cell of the AVN links with the first cell of the bundle. Initial conditions are shown in Table 3.

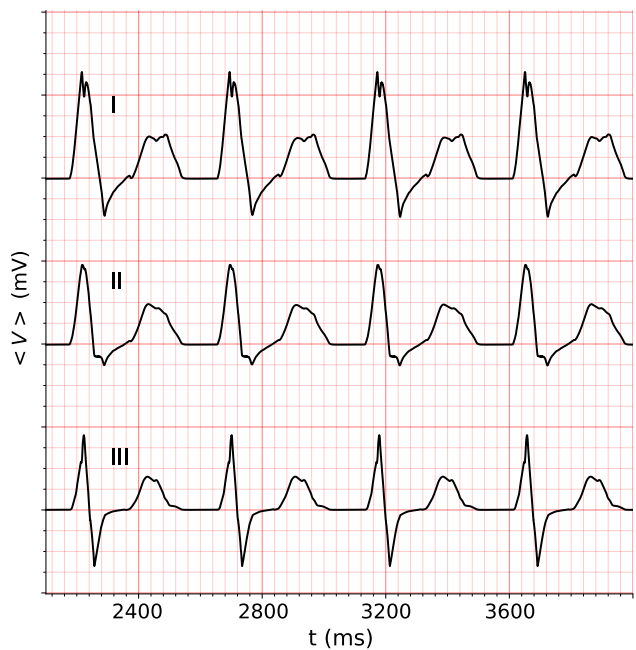


Figure 8: Simulated 3-lead ECG of the heart exhibits Atrioventricular Nodal Reentry Tachycardia, with the initial conditions presented in Table 3. The P-wave is only visible at the start before it becomes completely obscured by a repetitive sequence of QRS complexes followed by T-waves.

All of this is also depicted in the 3-lead ECG shown in figure 8. The standard three-wave ECG is replaced by a two-wave recording, with the P-wave obscured as it coincides with the QRS complex. This ECG signature is a definitive indicator that a patient is experiencing Atrioventricular Nodal Reentry Tachycardia. In this instance, the heart rate for this tachycardia is 150 bpm, while the



Table 3: Initial conditions and parameters for the simulated heart suffering from Atrioventricular Nodal Reentry Tachycardia.

cells	$V(t=0)$ (mV)	$n(t=0)$	$I$ ( $\mu\text{A}/\text{cm}^2$ )	$g_K$ (mS/ $\text{cm}^2$ )	$R$ ( $\text{k}\Omega\text{cm}^2$ )
$(25, 2 \leq y \leq 23)_{AVN}$	-10.95	0.17	0	36	0.223
$(6, 2)_{AVN}$	-10.95	0.17	0	36	0.00675(right), $\infty$ (left)
$P_{SAN} = (19, 19)_{RA}$	-10.95	0.17	2.95	36	0.00675
Ventricle cells	-10.95	0.17	0	16.54	0.00675
All other cells	-10.95	0.17	0	36	0.00675

Table 4: Initial conditions and parameters for the model heart suffering from Wolff-Parkinson-White syndrome.

cells	$V(t=0)$ (mV)	$n(t=0)$	$I$ ( $\mu\text{A}/\text{cm}^2$ )	$g_K$ (mS/ $\text{cm}^2$ )	$R$ ( $\text{k}\Omega\text{cm}^2$ )	extra connection
$(19, 56)_{RA}$	-10.95	0.17	0	36	0.00675	with $(19, 19)_{LA}$
$(19, 19)_{LA}$	-10.95	0.17	0	36	0.00675	with $(19, 56)_{RA}$
$P_{SAN} = (19, 19)_{RA}$	-10.95	0.17	2.95	36	0.00675	no
Ventricle cells	-10.95	0.17	0	16.54	0.00675	no
All other cells	-10.95	0.17	0	36	0.00675	no

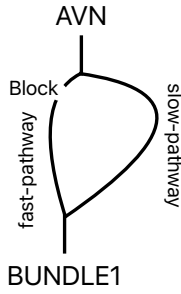


Figure 9: Diagram of the geometry of the internal structure of the Atrioventricular Node. The darker blue denotes the conductive pathways, whereas the cells depicted in lighter blue are zero-flux. The top and bottom points connect to both the AVN cell and BUNDLE1, respectively. The fast pathway shares the same resistivity as the other heart cells, while the slow pathway has a resistivity of  $R_{slow} = 0.223 \text{ k}\Omega \text{cm}^2$ . The uni-directionally blocked cell is marked in orange.

SAN is functioning at 60 bpm ( $I_{SAN} = 2.95 \mu\text{A}/\text{cm}^2$ ).

### 6.3 Accessory pathway

An accessory pathway is an undesirable connection between regions of heart tissue that can lead to issues with the coordination of muscle contraction. Wolff-Parkinson-White syndrome (WPW), a congenital condition, exemplifies a situation where excess tissue connects two parts of the conduction system that should be electrically isolated [Sapra *et al.*, 2020]. This syndrome is characterised by a connection between an atrium and a ventricle, resulting in the premature beating of the latter. In this instance, we focused on the connections on the right side of the human heart, specifically between the right atrium and the right ventricle. The initial conditions are detailed in Table 4, and the ECG results are depicted in Figure 10 in black, overlaid with the results from a healthy heart. Unsurprisingly, the QRS complex begins earlier than expected, leading to the delta wave, which is the primary feature of WPW syndrome.

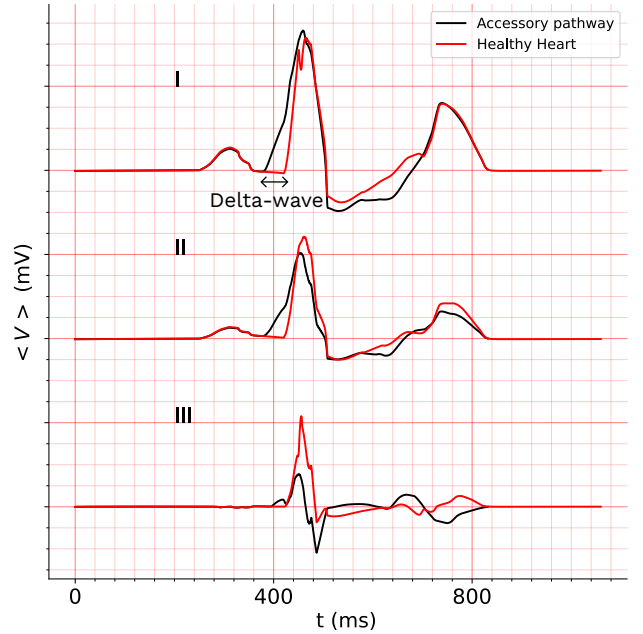


Figure 10: In black, a simulated 3-lead ECG of the heart, featuring an accessory pathway that connects the RA and RV is displayed. The initial conditions are outlined in Table 4. In contrast, the three-lead ECG of a healthy heart is shown in red. The key difference between the two is the early QRS complex known as the Delta-wave.

Table 5: Initial conditions and parameters for the model heart suffering from Ischemia on the right atrium.

cells	$V(t=0)$ (mV)	$n(t=0)$	$I$ ( $\mu\text{A}/\text{cm}^2$ )	$g_K$ ( $\text{mS}/\text{cm}^2$ )	$R$ ( $\text{k}\Omega\text{cm}^2$ )
$(25 \leq x \leq 50, 25 \leq y \leq 50)_{RA}$	-10.95	0.17	0	36	$(0.00675, 2.025]$
SAN $(19, 19)_{RA}$	-10.95	0.17	2.95	36	0.00675
Ventricle cells	-10.95	0.17	0	16.54	0.00675
All other cells	-10.95	0.17	0	36	0.00675

## 6.4 Ischemia-related arrhythmias

A lack of blood supply to myocytes can result in their death and, more importantly, an incomplete apoptosis process that renders gap junctions semi-functional [Yasui *et al.*, 2000]. Under these conditions, the connections between adjacent cells become inefficient, leading to a significant decrease in conduction velocities. These asymmetries in the muscular tissue may then cause the separation of wavefronts and ultimately result in re-entry, which leads to arrhythmic events.

To model this condition, a square region ( $25 \leq x \leq 50, 25 \leq y \leq 50$ ) was defined, where the resistivities of the gap junctions were randomly assigned between the standard  $0.00675 \text{ k}\Omega\text{cm}^2$  and an infinitely high resistivity, rendering the tissue dead and thus unresponsive. The random distribution was structured so that 80% of the cells within this interval were impaired, that is, with  $R \in (0.00675, 2.025] \text{ k}\Omega\text{cm}^2$  and 15% comprised of dead cells, while the remaining 5% were completely healthy. Furthermore, the level of impairment among the 80% is linearly related to the proximity to the centre of the scar: the closer a cell is to the centre of the square, the greater the probability that its gap junction resistivities will be elevated. Initial conditions are shown in Table 5.

As this ischemia is present in the RA, no significant changes in the overall shape of the ECG waves were anticipated, as this cavity contributes relatively little to the results of the leads. Aside from the increase in heart rate due to reentrant waves within the damaged tissue, we expected only the P-wave to exhibit a different shape, while both the QRS complex and the T-wave would remain similar to those of a healthy heart. However, as demonstrated in figure 11, this was not the case. Extremely irregular patterns emerged due to an issue with the excitation of the ventricles. Further work is required to ensure the correct connection with the ventricles.

## 7 Conclusions

In this paper, we introduce a new geometric whole-heart model, which includes the atria and ventricles. Each of the four cavities is modelled as a two-dimensional sphere through which electrical signals propagate via diffusion. In this paper, we introduce a novel geometric whole-heart model that encompasses the atria and ventricles. Each of the four cavities is represented as a two-dimensional sphere through which electrical signals propagate via diffusion. The connections between the atria are facilitated by the Bachmann bundle. The connections between the atria and ventricles are depicted by a one-dimensional cable representing the His and Purkinje fibres, as well as the atrioventricular node. With this model, we have managed to simulate the electrical properties and repolarisation dynamics across the heart's tissues. connec-

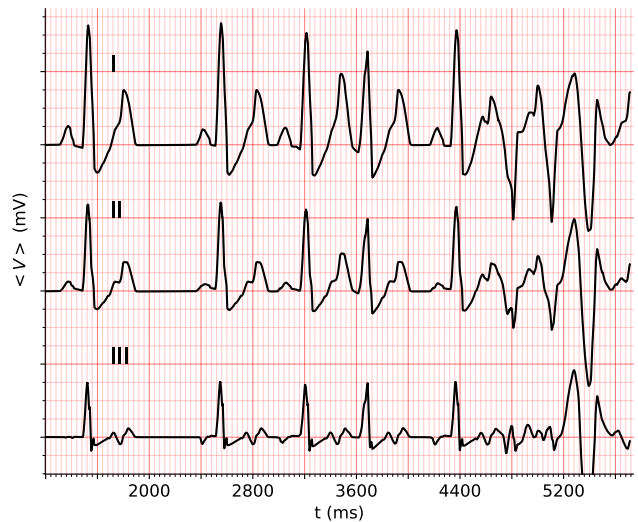


Figure 11: Simulated 3-lead ECG of the model heart experiencing ischemia on the RA, with initial conditions presented in Table 5. The regular ECG waves are replaced by irregular electrical signatures at  $t = 3040$  ms, due to reentry triggered by the damaged tissue.

tions between the atria are made through the Bachmann bundle. Connections between the atria and ventricles are represented by a one-dimensional cable modelling the His and Purkinje fibres and the atrioventricular node. With this model, we were able to simulate the electrical properties and repolarisation dynamics across the heart's tissues.

The electric stimulus of the heart is generated in the sinoatrial node through an action potential signal described by a simplified Hodgkin-Huxley type model, which features a single potassium-sodium gating variable. Adjustments to a current parameter of the sinoatrial node influence the heart rate. The temporal evolution of action potentials across the cardiac cells was simulated using Python. With this model, we obtained an in silico 3-lead electrocardiogram. Simulations have demonstrated that the 3-lead electrocardiogram closely aligns with the clinical data of healthy individuals. These results indicate that this model can be understood as a digital twin of the heart.

Based on these results, we have simulated several pathologies, deriving the electrophysiological map of the heart along with the corresponding 3-lead electrocardiogram. In particular, we were able to model the conditions leading to arrhythmias, ventricular tachycardia, atrioventricular nodal reentry tachycardia, accessory pathways, and ischaemia-related arrhythmias. Our results align with the generally observed ECG waves for the various pathologies studied, demonstrating that this model could serve as a valuable tool in studies of the human heart, providing ECG signatures that could validate the results against clinically obtained data. Given the relatively low process-

ing power required to operate this model, it is advantageous to analyse different pathological scenarios.

During the construction of the model, we encountered several challenges related to the various connections between the heart cavities, the initial conditions that resulted in abnormal propagation properties in the cardiac tissues, the generation of spiral waves, and the influence of myocytes' ionic gating variables. Improving our understanding of these anatomical and physiological processes could be a critical aspect of cardiac research.

**Acknowledgements:** We would like to thank Sérgio Laranjo and Pedro Cunha, cardiologists from Santa Marta Hospital in Lisbon, for introducing us to the dynamics and physiology of the heart. This article has gained from discussions with them and thorough reading. We also thank our colleague Teresa Pinheiro for her biological support and unwavering enthusiasm for this research.

## References

- [Alonso *et al.*, 2016] S. Alonso, M. Bär and B. Echebarria, Nonlinear physics of electrical wave propagation in the heart: a review, *Rep. Prog. Phys.* **79** (2016) 096601.
- [Atterhög & Loogna, 1977] J.-H. Atterhög and E. Loogna, P-r interval in relation to heart rate during exercise and the influence of posture and autonomic tone, *Journal of Electrocardiology* **10** (1977) 331-336.
- [Beaumont *et al.*, 1998] J. Beaumont, N. Davidenko, J. M. Davidenko and J. Jalife, Spiral waves in two-dimensional models of ventricular muscle: formation of a stationary core, *Biophysical Journal* **75** (1998) 1-14.
- [Beeler & Reuter, 1977] G. W. Beeler and H. Reuter, Reconstruction of the action potential of ventricular myocardial fibres, *The Journal of Physiology* **268** (1977) 177-210.
- [Branco & Dilão, 2024] L. Branco and R. Dilão, Interdependence of sodium and potassium gating variables in the Hodgkin-Huxley model, preprint, 2024, <http://arxiv.org/abs/2402.16711>.
- [Bueno-Orovio *et al.*, 2008] A. Bueno-Orovio, E. Cherry and F. Fenton, Minimal model for human action potentials in tissue, *J. Theo. Biol.*, **253** (2008) 544-560.
- [Courtemanche *et al.*, 1998] M. Courtemanche, R. J. Ramirez and S. Nattel, Ionic mechanisms underlying human atrial action potential properties: insights from a mathematical model, *American Journal of Physiology-Heart and Circulatory Physiology*, **275** (1998) 301-321.
- [Dilão, 2023] R. Dilão, Dynamical System and Chaos: An Introduction with Applications, Springer International Publishing, 2023.
- [Dilão & Sainhas, 1998] R. Dilão and J. Sainhas, Validation and calibration of models for reaction-diffusion systems, *International Journal of Bifurcation and Chaos* **8** (1998) 1163-1182.
- [Enderle & Bronzino, 2012] Enderle, J. and Bronzino, J., Introduction to biomedical engineering, Third edition, 2012.
- [Fedele *et al.*, 2023] M. Fedele, R. Piersanti, F. Regazzoni, M. Salvador, P. C. Africa, M. Bucelli, A. Zingaro, L. Dede, A. Quarteroni, A comprehensive and biophysically detailed computational model of the whole human heart electromechanics, *Comput. Methods Appl. Mech. Engrg.* **410** (2023) 115983.
- [Fridericia, 1920] L. S. Fridericia, Die systolendauer im elektrokardiogramm bei normalen menschen und bei herzkranken, *Acta Medica Scandinavica* **53** (1920) 469-486.
- [George *et al.*, 2017] S. George, F. Ndeye Rokhaya, A. Murillo-Berlioz, K. Lee, K. Kamiya, G. Trachiotis, I. Efimov, At the Atrioventricular Crossroads: Dual Pathway Electrophysiology in the Atrioventricular Node and its Underlying Heterogeneities, *Arrhythmia and Electrophysiology Review* **6** (2017).
- [Gillette *et al.*, 2022] K. Gillette, M. Gsell, M. Strocchi, T. Grandits, A. Neic, M. Manninger, D. Scherr, C. Roney, A. Prassl, C. Augustin, E. Vigmond and G. Plank, A personalized real-time virtual model of whole heart electrophysiology, *Frontiers in Physiology* **13** (2022).
- [Irisawa & Noma, 1982] H. Irisawa and A. Noma, Pacemaker Mechanisms of Rabbit Sinoatrial Node Cells. Dordrecht: Springer Netherlands, 1982, pp. 35-51.
- [Niederer *et al.*, 2022] S. Niederer, J. Lumens, and N. Trayanova, Computational models in cardiology, *Nature Reviews Cardiology* **16** (2018).
- [Noble, 1962] D. Noble, A modification of the Hodgkin-Huxley equations applicable to Purkinje fibre action and pacemaker potentials, *The Journal of Physiology*, **160** (1962) 317-352.
- [Olívia & Dilão, 2025] J. Olívia and R. Dilão, GitHub program, <https://github.com/jolivia1/Minimal-Heart-Model>.
- [Quarteroni *et al.*, 2022] A. Quarteroni, L. Dedè and F. Regazzoni, Modeling the cardiac electromechanical function: a mathematical journey, *Bulletin AMS* **59** (2022) 371-403.
- [Sapra *et al.*, 2020] A. Sapra, J. Albers, P. Bhandari, D. Davis and E. Ranjit, Wolff-Parkinson-White Syndrome: A Master of Disguise, *Cureus* **12**(6) (2020) e8672.
- [Singstad, 2022] B.-J. Singstad, Norwegian endurance athlete ECG database, *IEEE Open Journal of Engineering in Medicine and Biology* **3** (2022) 162-166.
- [Thangaraj *et al.*, 2023] P. M. Thangaraj, S. H. Benson, E. K. Oikonomou, F. W. Asselbergs and R. Khera, Cardiovascular care with digital twin technology in the era of generative artificial intelligence, *European Heart Journal* (2024).

- [Trayanova, 2011] N. Trayanova, Whole-heart modeling applications to cardiac electrophysiology and electromechanics, *Circulation research* **108** (2011) 113-128.
- [Viola *et al.*, 2023] F. Viola, G. Del Corso, R. De Paulis and R. Verzicco, GPU accelerated digital twins of the human heart open new routes for cardiovascular research, *Scientific Reports* **13** (2023).
- [Yasui *et al.*, 2000] K. Yasui, K. Kada, M. Hojo, J-K. Lee, K. Kamiya, J. Toyama, T. Ophtho and I. Kodama, Cell-to-cell interaction prevents cell death in cultured neonatal rat ventricular myocytes, *Cardiovascular Research* **48**(1) (2000) 68-76.